Networked Radar Systems for Cooperative Tracking of UAVs

Brady Anderson[1], Jaron Ellingson[2], Michael Eyler[3], David Buck[4],
Cameron K. Peterson[5], Tim McLain[6], and Karl F. Warnick[7]

***Abstract*— To enable expanded and safer access for unmanned aerial vehicles in the National Airspace System, a reliable system to detect and track them needs to be established. This paper combines two radar systems into a single network to provide tracking of UAVs across a wide area. Each radar detects the UAV's path and those detections are combined into tracks using a recursive random sample consensus algorithm. Outdoor flight experiments show the ability of the system to track a UAV across two different radar fields of view.**

I. Introduction

Access to the National Airspace System (NAS) for a wide array of commercial and private parties with Unmanned Aerial Vehicles (UAVs) will benefit society by enabling UAV use for package delivery [1], security and defense [2], medicine [3], and recreation [4]. To enable safe operation of potentially dense traffic, as analyzed by [4], a system guaranteeing collision avoidance needs to be implemented. To effectively ensure this guarantee, full knowledge of activity in the airspace needs to be achievable, with some degree of forecasting the expected behavior of airspace occupants. This work presents a system that can detect and track airspace obstacles, especially UAVs, for planned integration into NASA's Unmanned Aircraft System (UAS) Traffic Management (UTM) System.

A significant amount of research has investigated the benefits of using multiple radar sensors. Combining detections from multiple radars to gain greater accuracy has been discussed in [5]–[8]. Methods to detect and track targets with traditional, single-transceiver radars are well established and have been used for UAS applications [9]–[13]. In addition, a variety of algorithms have been developed to best understand how to process radar data [13]–[19]. Recursive Random Sample Consensus (R-RANSAC) is one such algorithm and was developed in [18]. R-RANSAC operates by determining valid target models that fit acquired measurements. This paper expands upon that by applying the algorithm to multiple radar units in a network simultaneously.

These radar platforms were used together to form a radar sensor network (RSN). RSNs were also used in [5]–[8]. McLaughlin, et al. [5] discussed the feasibility of using a network of low C-SWAP radars to detect meteorological data in the low-altitude airspace over the country which could supplement traditional, long-range radars. Dutta, et al. [6] built physical devices and networked them together. They used the detections to track ground targets such as cars and people, but only up to 20 meters (m) away.

Both Liang, et al. [7] and Bartoletti, et al. [8] discussed the advantages of using a network of radar sensors for tracking. Laing, et al. [7] demonstrated the increased robustness of target tracking with a network of radar sensors when compared to a single radar. Bartoletti, et al. [8] looked into the design of these networks to improve the detection of targets and decrease uncertainty. However, in both cases their results were limited to simulations.

[9]–[13] performed testing with physical radar systems. The study by Silver et al. [9] performed testing with a ground-based GPS reflectometry radar receivers and found they were able to identify buildings in their field of view (FOV) using their passive sensor. Chan et al. [10] utilized radar data collected from F/A-18 radar systems to demonstrate the better accuracy of a fuzzy-gain filter when compared to a two-stage Kalman filter (traditionally used for target tracking). It also did not require any target dynamics to track them. However, their radar had a low scanning rate (10 seconds), which increases the amount of target uncertainty. Another study, Park et al. [11], used multiple radars and analyzed the collected data using clustering. That study also relied on provided altitude information to fully document the targets, an assumption that is not generally feasible.

Several studies [13]–[19] have focused on the algorithms used for detecting and tracking targets. [14] used a low (C-SWAP) weather radar in conjunction with a Kalman filter, reiterative minimum mean square error, and joint probabilistic data association to clarify the data. However, the study ran into issues due to slow mechanical scanning and a limited FOV. An older study by Reid [15] used clustering to help identify tracks, sort data, and then simulated it with a single sensor.

Cook et al. [16], [17] showed the use of fuzzy logic

*This material is based upon work supported by the National Science Foundation under Grant No. 1727010. This work is also supported by the Center for Unmanned Aircraft Systems (C-UAS), a National Science Foundation Industry/University Cooperative Research Center (I/UCRC) under NSF award No. IIP-1161036 along with significant contributions from C-UAS industry members.

[1] Brady Anderson is a PhD candidate in the Department of Mechanical Engineering, Brigham Young University b.anderson@byu.edu

[2] Jaron Ellingson is an MS candidate in the Department of Mechanical Engineering, Brigham Young University jaronce@byu.edu

[3] Michael Eyler is an MS candidate in the Department of Electrical Engineering, Brigham Young University michael.eyler@byu.edu

[4] David Buck is a PhD candidate in the Department of Electrical Engineering, Brigham Young University buckd@byu.edu

[5] Cameron K. Peterson is an Assistant Professor in the Department of Electrical and Computer Engineering, Brigham Young University cammy.peterson@byu.edu

[6] Tim McLain is a Professor in the Department of Mechanical Engineering, Brigham Young University mclain@byu.edu

[7] Karl F. Warnick is an Assistant Professor in the Department of Electrical and Computer Engineering, Brigham Young University warnick@byu.edu

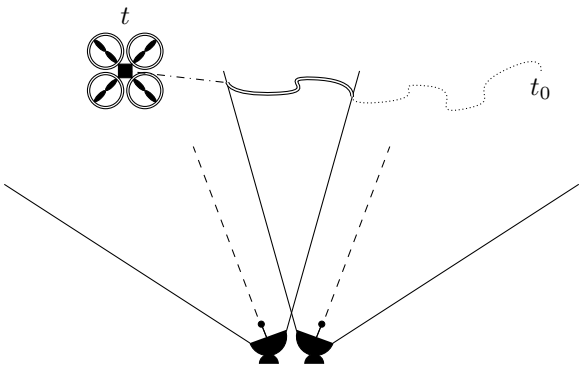

Fig. 1. The dash-dotted line is the left radar track (ending at time t), the dotted line is the right radar track (beginning at time t_0), and the double line represents the combined tracks. The R-RANSAC algorthim provides the framework for continuous tracking of the aerial vehicle, providing for wider coverage.

for target tracking and state estimation. [16] was able to track all of their targets with an accuracy of less than 8.7 m. However, it was limited by a low sweep rate of three seconds (s). [17] demonstrated an improved accuracy of UAVs location estimation through fusing the data of multiple sensors (including radar) over the accuracy of any single sensor.

This work expands on [18], [19], and on previous work in [13] which used variants of R-RANSAC. [18] introduced R-RANSAC and presented the algorithm's feasibility with a few simulations. [19] applied this algorithm to visual tracking of multiple targets. In this work, the algorithm will be used for tracking with radar detections, as was also the case in [13].

The radar platform used in this work has also been utilized in previous work by the authors as a part of a Local Air Traffic Information System (LATIS). In [12], the radar was mounted to a UAV and multiple UAV fly-bys were used to create a repository of midair encounters to provide data to the community. The same radar platform was used on the ground to detect, track, and avoid potential collisions between a UAV and multiple intruders [13].

In summary, the work presented in this paper builds on former contributions in [13] and [12], which include the usage of low C-SWAP phased-array radars as active sensors and using the R-RANSAC algorithm for target tracking. These sensors are capable of detecting UAVs at distances of up to 100 m away and can detect multiple targets in the presence of noisy measurements.

The capabilities of target detection and tracking were further extended in this work by combining multiple radars within a network to cover an arbitrarily large area. The data is then combined for a better understanding of the aerial targets, as briefly described in Figure 1.

The remainder of the paper will proceed as follows: Section II contains the methods used to perform the experiments and collect the results. Section III includes the results from in-field flight experiments. Finally, Section IV reviews the conclusions made from these results and future directions that can be explored.

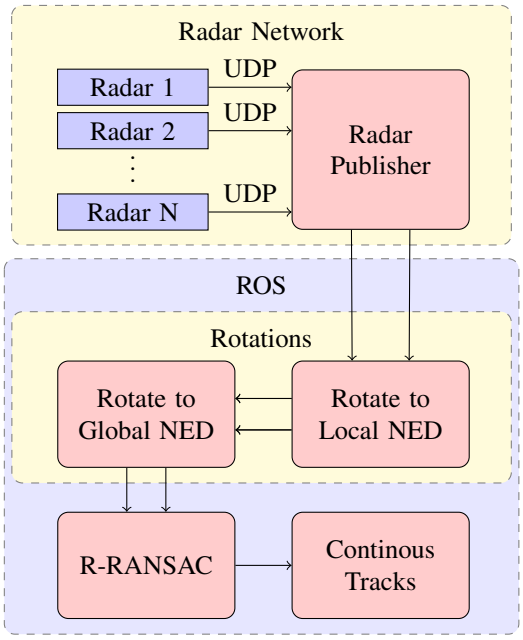

Fig. 2. Block diagram of the data flow from separate radar inputs to one continuous track.

II. Methods

This section will outline data flow from the radar detections to continuous tracks as illustrated by Figure 2. Subsection II-A explains the design of the radars which publish range and bearing measurements of possible targets to the network over User Datagram Protocol (UDP). The UDP messages are received, parsed, and broadcast on a robot operating system (ROS) network for further analysis. Next, Subsection II-B will highlight how the range and bearing data are converted into a local north-east-down (NED) Cartesian frame (Equation (6)) and then rotated into a global NED frame through rotations determined by a calibration process (Equation (7)). Finally, Subsection II-C will review how R-RANSAC takes the global NED measurements from both radars to produce one continuous track.

A. Radar

To track UAVs, the local RSN uses X-Band phased-array radar systems developed at Brigham Young University. These systems use 2 ms linear frequency-modulated continuous-wave (FMCW) sawtooth pulses, which repeat at a rate of approximately 450 Hz. The FMCW pulses reflect off targets and are received by four spatially-separated antennas which form a phased-array (see Figure 3). Phased arrays are used to provide direction-of-arrival (DOA) estimation without needing to move and aim the antenna. After being received by the antennas, and at each of the four channels, the signals are down-mixed with the transmit pulse to base-band, which generate beat frequencies of possible targets that are linear with distance. These signals are filtered,

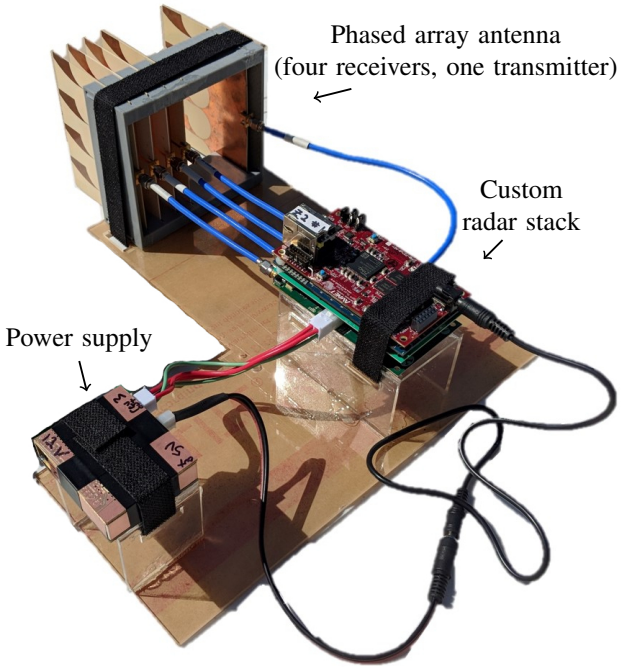

Fig. 3. X-band phased array radar used in field experiments.

amplified, and digitally sampled at 2 Mega-samples per second (Msamples/sec).

After sampling, a field programmable gate array (FPGA) further processes the data by running a fast Fourier transform (FFT) to separate signal power into range bins. These range bins are cross-correlated across each of the four channels and averaged over 32 pulses before being sent to the CPU. The CPU takes the averaged correlation data from the FPGA and runs target detection and DOA estimation algorithms to generate a list of targets with their range and bearing. This list is sent to the ROS network over a UDP connection as shown in Figure 2.

Some challenges with radar include the various ways noise and interference can introduce false targets or inaccurate range and angle estimation. False targets can arise from in-band interference or large power returns that rail the amplifiers. Inaccurate range estimation can arise from multi-path scenarios, such as a ground-bounce. Inaccurate angle estimation can come from anything that introduces phase differences between the channels such as phase noise in the radar electronics, inferior performance of a channel, or the angle sensitivity due to longer distances of a target in a polar coordinate system.

B. Calibration

System calibration involves defining the rotation between the radar's body-fixed frame and a larger, common frame. The body-fixed frame of the radar is defined by aligning the $-\mathbf{z}$-axis with the radar boresight vector. Further, the body-fixed $+\mathbf{y}$-axis is defined by zero degrees azimuth, and the frame is completed by defining the $+\mathbf{x}$-axis using the right-hand rule. The larger, common frame is an inertial NED frame based off a tangent plane on the geodetic ellipsoid. The origin of this plane is located at the earth-centered, earth-fixed (ECEF) position of a user-selected base radar station, and is aligned with the local cartographic map.

The calibration for each radar is accomplished by solving the orthogonal Pocrustes problem [20] to find the rotation $\mathbf{R_{cal}}$ between the body-fixed radar frame and the local NED inertial frame. The orthogonal Procrustes problem takes two sets of data as inputs: a time history of a known vehicle's local NED measurements converted from RTK-GPS, $\mathbf{A} \in \mathbf{R}^{3\times n}$, and correspondingly, time-synced radar target estimates, $\mathbf{B} \in \mathbf{R}^{3\times n}$, where n is the number of synced measurements. Synced measurements are radar detections that correspond with RTK-GPS measurements within a prescribed time and range tolerance.

The time tolerance defines the maximum temporal separation allowed between detections from the radar and positional reports from the vehicle. For example, if the vehicle reports its position at 2.43 s, the radar reports a set of detections at 2.41 s, and the time tolerance is 0.03 s, these sets of points are considered temporally paired. These points are then pruned a second time using a spatial range tolerance parameter. The range returned by the radar at that reported time must be within the spatial tolerance of the euclidean distance between the radar and vehicle's RTK-GPS positions. If both of these conditions hold, it is considered a paired point for use as an input to the orthogonal Procrustes problem. Temporal and spatial bounds were tuned to 0.01 s and 3 m for the ground test, and 0.08 s and 4 m for the aerial tests. Tighter bounds were required for the ground tests to account for increased clutter.

Figure 4 presents the overall process of calibration using high resolution RTK-GPS on both the ground station radar and the vehicle.

To place both of these sets of data in the same frame, we first define the origin of the local NED inertial frame. This is done by measuring the latitude (ϕ), longitude (λ), and altitude (h) of the radar base station using RTK-GPS. These geodetic coordinates are then converted into the ECEF frame by the following equations [21]:

$$x = (N(\phi) + h)\cos(\phi)\cos(\lambda) \tag{1}$$

$$y = (N(\phi) + h)\cos(\phi)\sin(\lambda) \tag{2}$$

$$z = \left(\frac{b^2}{a^2}N(\phi) + h\right)\sin(\phi) \tag{3}$$

$$N(\phi) = \frac{a^2}{\sqrt{a^2\cos^2(\phi) + b^2\sin^2(\phi)}} \tag{4}$$

where a is the semi-major axis and b is the semi-minor axis of the ellipsoid (earth).

High precision vehicle RTK-GPS positions recorded over the course of the test are similarly converted to the ECEF

frame. These ECEF positions are then expressed in the local NED inertial frame by using

$$\mathbf{p}_{NED} = \mathbf{R}_{\text{n/e}} \left(\mathbf{p}_{ECEF} - \mathbf{p}_{Ref} \right), \tag{5}$$

developed in [22], where $\mathbf{p}_{ECEF}$ is the ECEF position of the vehicle, and $\mathbf{p}_{Ref}$ is the ECEF position of the reference origin assigned to the position of the base radar station. The rotation $\mathbf{R}_{\text{n/e}}$ is defined as

$$\mathbf{R}_{\text{n/e}} = \begin{pmatrix} -\sin\phi\cos\lambda & -\sin\phi\sin\lambda & \cos\phi \\ -\sin\lambda & \cos\lambda & 0 \\ -\cos\phi\cos\lambda & -\cos\phi\sin\lambda & -\sin\phi \end{pmatrix}, \tag{6}$$

where ϕ and λ are the geodetic latitude and longitude corresponding to the position of the NED frame origin.

The next preparation step before computing the calibration rotation matrix is to express the radar detections in the local NED inertial frame. The vehicle is flown in front of the radar, and the radar records possible targets in polar coordinates of range and bearing. These coordinates are upsampled to spherical coordinates using range, zenith, and azimuth. Zenith is defined off the radar's boresight and azimuth is measured CCW around boresight in a right-hand manner.

Due to the current setup using a 1-D radar system, azimuth is assigned as 0 or π depending on the sign of bearing. Zenith is then assigned as the absolute value of the bearing measurement. With the targets now in spherical coordinates, a traditional spherical to 3-D Cartesian transformation is used to place the targets in the body-fixed radar frame.

At this point the RTK-GPS positions and the radar targets are in Cartesian coordinates with a common origin at the base radar station. As stated earlier, the GPS measurements are denoted by the matrix **A** and the converted radar detections by **B**. Both are $3 \times n$ matrices where the columns are time stamped $[x,\ y,\ z]^T$ measurements.

Where this is the calibration step, we take advantage of our full knowledge of the system. We first assume that our calibration pass with the target was slow enough that any radar detection within a tolerance of 0.01 s (this changed slightly for different tests, see results in Section III) of a GPS measurement was a time matched data point. We further pruned clutter from the detections by requiring that these time matched detections be within 3 or 4 m of a range calculated from the GPS data. As seen by the well defined path in Figure 8, this was sufficient to remove almost all clutter from the radar detection dataset. These pruned **A** and **B** matrices are then used as inputs to the orthogonal Procrustes problem.

$$\mathbf{R}_{\text{cal}} = \underset{\Omega}{\operatorname{argmin}} ||\Omega\mathbf{A} - \mathbf{B}||_F, \tag{7}$$

where Ω is a unitary matrix that produces the minimum of the argument in (7) and $||\cdot||_F$ represents the Frobenius norm. This produces the rotation matrix from the inertial NED frame to the radar frame, $\mathbf{R}_{\text{cal}}$. The transpose, $\mathbf{R}_{\text{cal}}{}^{\text{T}}$, is used to rotate all the radar detections, including clutter, into the inertial frame aligned with the cartographic map.

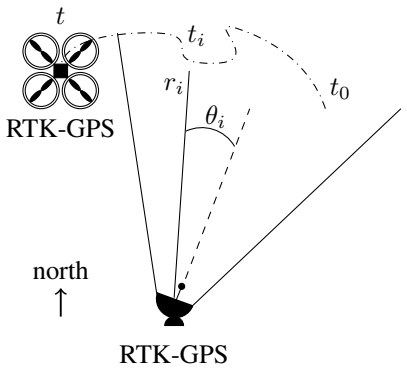

Fig. 4. The dash-dotted line is the path of the vehicle and the dashed line is the boresight of the radar. For calibration, the vehicle and radar are each located by using high precision RTK-GPS measurements to create the tracks within their respective frames. Where r_i and θ_i denote a range and angle off boresight at a time t_i between t_0 and t. The Procrustes algorithm allows alignment of the radar targets with the global NED frame.

The detections in the inertial frame become the input to the R-RANSAC algorithm.

C. R-RANSAC

Once calibration has been performed, the R-RANSAC algorithm determines which measured targets are tracks from the vehicle. R-RANSAC is based largely on the work done in [13] and is not newly developed in this paper but is applied to this unique application. In general, R-RANSAC operates using RANSAC to create tracks that fit a tuned model, then propagates those tracks with a tuned Kalman filter. A brief overview of the primary tuning variables is discussed here, but for an in-depth understanding, the reader is referred to the literature.

Detections from multiple radars are used as simultaneous inputs to R-RANSAC at each time step. If any subset of points fit a good track as determined by RANSAC, they are grouped by fit models and each of these models is propagated as an active target detection. This process ideally eliminates all noise and clutter from the radar detections, reporting only positions of real vehicles or other obstructions in the FOV of the radar.

Four R-RANSAC parameters are tuned for this work. The first parameter is the maximum number of models retained by R-RANSAC, $\mathcal{M}$. This is not the max number of "good" models, but the maximum number of potential models to propagate. A low number of targets is expected, thus this parameter was set low. The next parameter is the number of consecutive missed detections, CMD, allowed before a track is considered unstable and no longer propagated. CMD is set low to better prune clutter in the radar returns. The third parameter is the lifetime threshold, τ_T. It defines the minimum lifetime of a model before it is considered good enough to propagate. We relied on the idea that real detections are more consistent than clutter, and have a longer lifetime. The final parameter is the inlier region threshold, τ_R, which determines if measurements fit the model. This is also set low to reflect the cohesive nature of detections of a

moving target, as opposed to the more random nature of the clutter. The following values were used: $\mathcal{M} = 5$, $CMD = 3$, $\tau_T = 4$, and $\tau_R = 8$.

III. Results

Two separate tests were conducted to track targets across two partially overlapping FOVs from two radars. In both cases, the vehicle target recorded RTK-GPS latitude, longitude, and altitude, whether on the ground or in the air. This information was used as truth data for radar attitude calibration and for verification of final R-RANSAC results. Also, the RTK-GPS positions of the radars were recorded at the beginning of the test to calculate the proper transformation of vehicle positions from ECEF to a local NED Cartesian coordinate system with the origin set at the location of the first radar.

The first test involved a human walking along the ground carrying an RTK-GPS unit and a corner reflector for a bright radar target. The second test was conducted with a hand-operated remote control airborne target vehicle. This vehicle was an X-8 octorotor with a breadth of approximately 0.5 m^2 and a height of 0.25 m. The vehicle had a small corner reflector which was aimed in the general direction of the radars for the duration of the flight.

The rest of this section will compare the ground test results with the aerial results for each of the three stages of data analysis: (a) collecting of raw radar detections, (b) calibration of radar frames, and finally (c) using R-RANSAC to filter raw detections by tracking likely sequences of true target movements. Figures 5 and 6 show the pre-calibrated results from the radar (step a) which is in direct comparison to the calibrated plots in Figures 7 and 8 (step b). Finally, Figures 9 and 10 show the R-RANSAC reporting a continuous track from the two radars (step c).

The calibration step had to be computed for both tests for two reasons. The first is that since each test happened on different days, the radars were not mounted in the exact same spots both days, nor with the same attitude. Compounding the difference in attitude is that, since the radars only report targets in two dimensions, they can only track and report targets in a mostly flat fan shaped FOV. To track targets on the ground, the radars have to be pointed down, as opposed to being pointed up to track the aerial vehicle in the second test. The calibration step allows computation of an accurate rotation from the cartographically aligned local NED inertial frame into the radar's body fixed frame in both cases. Thus, the data in the figures that follow have all been projected onto the N-E plane, removing altitude information from the aerial test plots.

In addition to the GPS position of the target, Figures 5 and 6 shows unfiltered radar detections plotted with respect to their own axes. In this frame, the radar FOVs are aligned. Without calibration, the radars only know the positions of the detections with respect to themselves. The ground test shows much more clutter due to trees and other ground-level items creating false target detections. This condition required slightly tighter tolerances for time-syncing and

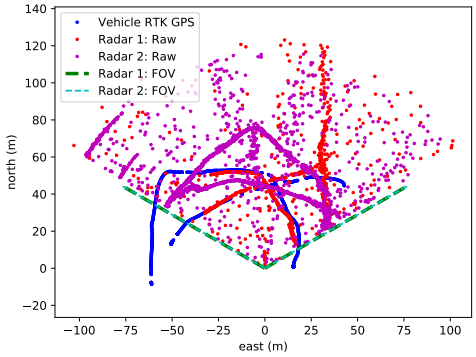

Fig. 5. Overlaid FOVs of pre-calibrated radars with GPS of a ground target.

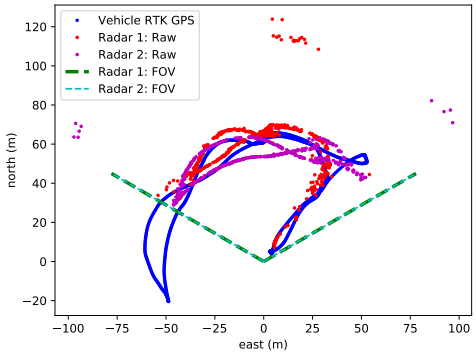

Fig. 6. Overlaid FOVs of pre-calibrated radars with GPS of an aerial target.

pruning during the calibration step, as opposed to the aerial tests. The final target detections were produced using the same R-RANSAC parameters for all tests.

Also visible in Figures 5, 6 and 9 are narrow bands at regular intervals which is interference caused by ground-to-air communication. We are using a high-powered Ubiquiti 5.8 GHz Wi-Fi system that that causes the radar to generate false targets when the Ubiquiti transmitter beam, or large reflections from it, are received by the radar antennas. This interference occurs because the radar's wide-band antennas easily receive the Wi-Fi signals. There is also a lack of RF filtering in the receive channels which allows mixing products to be aliased and digitally sampled. We lowered the Wi-Fi power to minimize this noise, but to properly resolve these interference issues, narrow-band antennas and an X-band band-pass filter in the receive chain are being developed.

With full knowledge of the system during the calibration step, the pruning, as described in Section II, is very accurate. Figures 7 and 8 show only radar detections that satisfies the pruning criteria of the time and range tolerances. The only axes shown are the N-E inertial axes. By pairing each radar's detections with the GPS data, an accurate rotation matrix is achieved for each radar, allowing each to report its targets correctly in the NED inertial frame. R-RANSAC receives

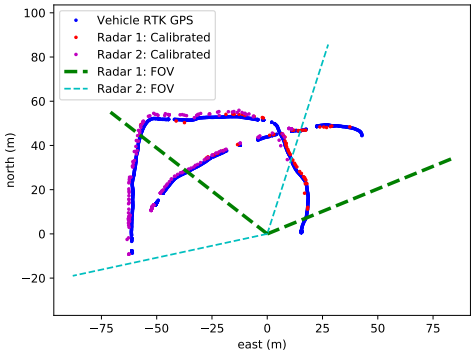

Fig. 7. The calibrated radar sightings with the ground target.

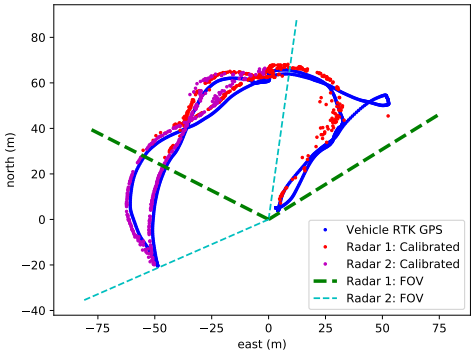

Fig. 8. The calibrated radar sightings with the aerial target.

all radar detections properly mapped in a common frame, allowing association of duplicate measurements in the areas where the FOVs overlap. The aerial plot (Figure 8) shows a small loop on the right with no radar detections. This is due to the vehicle being too low and thus out of view of the thin, 2-D radar FOV.

Figures 11 and 12 give us confidence in our calibration. Figure 11 shows radar detections from a second aerial test on the inertial NED frame. These were calibrated with a rotation matrix created by matching themselves with the second flight's GPS data. Figure 12 shows the same detections and GPS data from the second flight, however the radar detections were rotated into the inertial frame using the rotation matrix computed from the first aerial flight's calibration. There is a slight rotation offset visible between these two plots, reflecting small shifts in the radar stands used for these tests, which were not rigidly mounted. Over time, the mounts are prone to induce small attitude deviations due to equipment shifts and environmental factors. Regardless, the closeness of these datasets demonstrates a promising result for the use of a long term calibration of rigidly mounted radar units.

To simulate a more real-world scenario, the full radar dataset with no pruning was used with R-RANSAC. Figures 9 and 10 show that most clutter is removed by the tuned

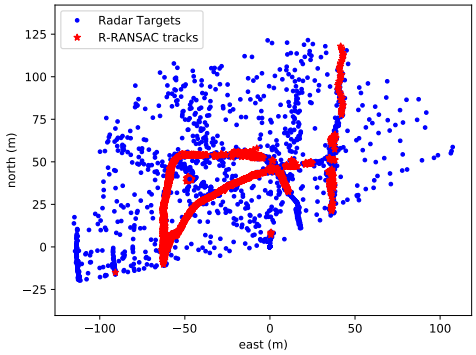

Fig. 9. R-RANSAC tracks with ground target. Note that a semi-truck drives past the radar during this test, which is seen by the linear group of tracks at approximately 40 meters east of the origin.

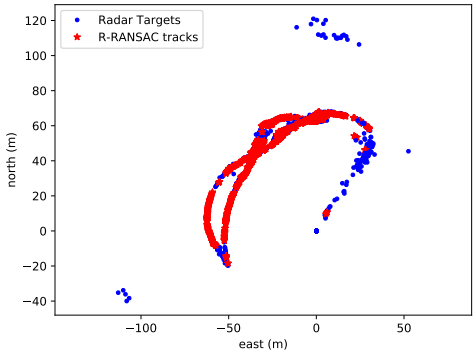

Fig. 10. R-RANSAC tracks with aerial target.

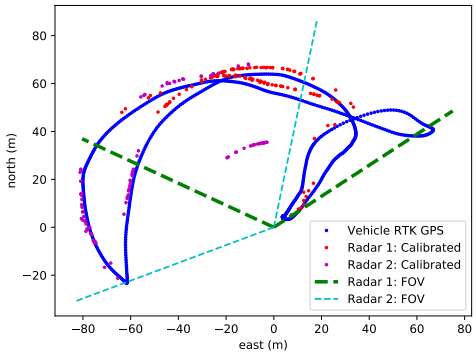

Fig. 11. Visual calibration verification created for a second aerial test using its own computed $\mathbf{R}_{\mathbf{cal}}$.

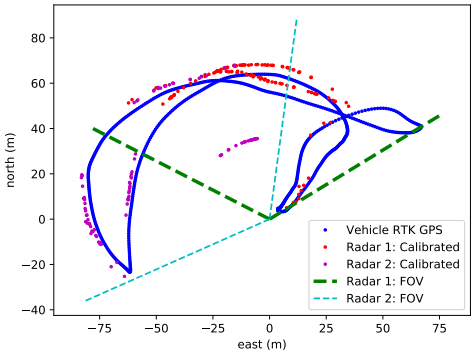

Fig. 12. Visual calibration verification created for a second aerial test using the $\mathbf{R}_{\mathbf{cal}}$ computed from the first aerial test data.

R-RANSAC tracker. These plots only use the GPS positions of the target as a truth verification tool, and demonstrate the consistent tracks reported by R-RANSAC are accurate.

Figure 9 shows a linear track at approximately 40 m to the east of the radars. This was a semi-truck that entered the radar's FOV during testing. R-RANSAC correctly identified it as a likely track due to the consistency of the radar returns. Both figures show that R-RANSAC accurately groups the targets from both radars in the common FOV as a single track.

IV. Conclusion

This work demonstrates that R-RANSAC can be used to accurately track multiple targets across overlapping radar FOVs. While air detections are much easier, due to significantly reduced clutter (i.e., false returns) in the target information reported by the radars, ground tracking is still accurate and possible. Successful aerial tests demonstrate the feasibility of the current radar platform for continued development of NAS applications. A 3-D radar is currently under development to allow expanded coverage. Further work will investigate the feasibility of calibration in real-time without GPS.

References

[1] Joshuah K Stolaroff, Constantine Samaras, Emma R ONeill, Alia Lubers, Alexandra S Mitchell, and Daniel Ceperley. Energy use and life cycle greenhouse gas emissions of drones for commercial package delivery. *Nature communications*, 9(1):409, 2018.

[2] Noel Sharkey. The automation and proliferation of military drones and the protection of civilians. *Law, Innovation and Technology*, 3(2):229–240, 2011.

[3] Timothy Amukele, Paul M Ness, Aaron A.R. Tobian, Joan Boyd, and Jeff Street. Drone transportation of blood products. *Transfusion*, 57(3):582–588, 2017.

[4] Federal Aviation Administration (FAA). FAA Aerospace Forecast: Fiscal Years 2019-2039. 2019.

[5] David McLaughlin, David Pepyne, et al. Short-wavelength technology and the potential for distributed networks of small radar systems. *Bulletin of the American Meteorological Society*, 90(12):1797–1818, 2009.

[6] Prabal K Dutta, Anish K Arora, and Steven B Bibyk. Towards radar-enabled sensor networks. In *2006 5th International Conference on Information Processing in Sensor Networks*, pages 467–474. IEEE, 2006.

[7] Jing Liang and Qilian Liang. Design and analysis of distributed radar sensor networks. *IEEE Transactions on Parallel and Distributed Systems*, 22(11):1926–1933, 2011.

[8] Stefania Bartoletti, Andrea Conti, and Andrea Giorgetti. Analysis of UWB radar sensor networks. In *2010 IEEE International Conference on Communications*, pages 1–6. IEEE, 2010.

[9] Randy Silver, Yan Rockee Zhang, Hernan Suarez, Yu Pan, and Yih-Ru Huang. GNSS-based passive radar sensing using hybrid-aperture system. In *Radar Sensor Technology XVII*, volume 8714, page 871409. International Society for Optics and Photonics, 2013.

[10] Keith C.C. Chan, Vika Lee, and Henry Leung. Radar tracking for air surveillance in a stressful environment using a fuzzy-gain filter. *IEEE Transactions on Fuzzy Systems*, 5(1):80–89, 1997.

[11] Chunki Park, Hak-Tae Lee, and Bassam Musaffar. Radar data tracking using minimum spanning tree-based clustering algorithm. In *11th AIAA Aviation Technology, Integration, and Operations (ATIO) Conference, including the AIAA Balloon Systems Conference and 19th AIAA Lighter-Than*, page 6825, 2011.

[12] Hunter G McClelland, Changkoo Kang, Craig A Woolsey, Adam K Roberts, David Buck, Thomas Cheney, and Karl Warnick. Small aircraft flight encounters database for UAS sense and avoid. In *AIAA Information Systems-AIAA Infotech@ Aerospace*, page 1152. 2017.

[13] Jared K Wikle, Timothy W McLain, Randal W Beard, and Laith R Sahawneh. Minimum required detection range for detect and avoid of unmanned aircraft systems. *Journal of Aerospace Information Systems*, pages 351–372, 2017.

[14] Ramesh Nepal, Yan Zhang, and William Blake. Sense and avoid airborne radar implementations on a low-cost weather radar platform. *Aerospace*, 4(1):11, 2017.

[15] Donald Reid. An algorithm for tracking multiple targets. *IEEE Transactions on Automatic Control*, 24(6):843–854, 1979.

[16] Brandon Cook, Timothy J Arnett, Owen Macmann, and Manish Kumar. Real-time radar-based tracking and state estimation of multiple non-conformant aircraft. In *AIAA Information Systems-AIAA Infotech@ Aerospace*, page 1133. 2017.

[17] Brandon Cook and Kelly Cohen. Multi-source sensor fusion for small unmanned aircraft systems using fuzzy logic. In *2017 IEEE International Conference on Fuzzy Systems (FUZZ-IEEE)*, pages 1–6. IEEE, 2017.

[18] Peter C Niedfeldt and Randal W Beard. Recursive RANSAC: multiple signal estimation with outliers. *IFAC Proceedings Volumes*, 46(23):430–435, 2013.

[19] Jeffrey Millard and Randy Beard. Improved track continuity in multi target tracking by fusing multiple input sources. In *2018 Annual American Control Conference (ACC)*, pages 1901–1906. IEEE, 2018.

[20] Peter H Schönemann. A generalized solution of the orthogonal Procrustes problem. *Psychometrika*, 31(1):1–10, 1966.

[21] Weikko A. Heiskanen. *Physical geodesy*. W.H. Freeman, San Francisco, 1967.

[22] Guowei Cai, Ben M Chen, and Tong Heng Lee. *Unmanned rotorcraft systems*. Springer Science & Business Media, 2011.